World Scientific
www.worldscientific.com

AN AXISYMMETRIC INCOMPRESSIBLE LATTICE BOLTZMANN MODEL FOR PIPE FLOW

T. S. LEE*, HAIBO HUANG† and C. SHU

Department of Mechanical Engineering
National University of Singapore, Singapore
10 Kent Ridge Crescent, Singapore 119260
*mpeleets@nus.edu.sg
†g0301108@nus.edu.sg

In this paper an accurate axisymmetric lattice Boltzmann D2Q9 model is proposed to simulate the steady and pulsatile flows in circular pipes. Present model is derived from an incompressible D2Q9 model and some errors in a previous model [Halliday *et al.*, *Phys. Rev. E* **64**, 011208 (2001)] are revised. In the previous model, some terms relative to the radial velocity are missing and would lead to large error for constricted or expanded pipe flows. Present model is validated by cases of laminar steady flow through constricted tubes and 3D Womersley flow. Comparing with the previous model, our model is much more accurate for steady flow in constricted circular pipes. For 3D Womersley flow, it is also observed that the present model can reduce the compressibility effect in previous model.

Keywords: Lattice Boltzmann method; axisymmetric; incompressible Navier–Stokes equation; pipe.

1. Introduction

The lattice Boltzmann method (LBM) has been proposed as an alternative numerical scheme for solving the incompressible Navier–Stokes (NS) equations.[1,2] Among different lattice Boltzmann equation (LBE) models in application, the Lattice Bhatnagar-Gross-Krook (LBGK) model is the simplest one because it only has one scalar relaxation parameter and a simple equilibrium momentum distribution function.[3] Here our axisymmetric LBM is derived from LBGK D2Q9 model.

It is sure that 3D LBM can directly handle the axisymmetric flow problems.[4−6] For the problems of 3D steady axisymmetric flows[5,6] or 3D axisymmetric unsteady flow[4] in straight tube, most of previous studies[4−6] recourse to the 3D LBGK model and using the 3D cubic lattices with proper curvature wall boundary treatment directly. That means a large mesh size and it is not so efficient to simulate an axisymmetric flow problem in that way. To simulate the aixsymmetric flows more efficiently, in 2001, Halliday *et al.*[3] proposed an axisymmetric D2Q9 model for the

3D axisymmetric flow problems and it seems very successful for simulation steady flow in straight tube. The main idea of the model is inserting several spatial and velocity dependent "source" terms into the microscopic evaluation equation for the lattice fluid's momentum distribution.[7] Halliday *et al.*[3] claimed the adjusted microscopic evaluation equation can recover the cylindrical polar coordinate form of the continuity and Navier–Stokes equations.

However, we found that some important terms relative to the radial velocity are missing in the axisymmetric D2Q9 model of Halliday *et al.*[3] Although the terms would have very small effect on simulation the flows in straight pipe, missing the terms would lead to large error for simulation the constricted or expanded pipe flows.

On the other hand, as we all know, through the Chapman-Enskog procedure,[8] a LBE can recover the incompressible Navier–Stokes equation successfully if the density fluctuation can be neglected. However, the density may fluctuate to a great extent in flows with large pressure gradient because the pressure and density variations satisfy the equation of states of an isothermal gas given by $\Delta p = c_s^2 \Delta \rho$,[8] where c_s^2 is a constant. In many previous studies,[4,8−10] the compressibility effect of standard LBGK model has been highlighted.

Since Halliday *et al.*[3] derived the axisymmetric model from standard LBGK D2Q9 model, the model's compressibility effect would inherit from the standard LBGK D2Q9 model. To derive a more accurate axisymmetric model, our derivation would begin from the incompressible LBGK D2Q9 model proposed by He and Luo.[9] The incompressible LBGK model was validated by steady plane Poiseuille flow and the unsteady 2D Womersley flow. In their model, the compressibility effect of the order $O(M_2)$ is explicitly eliminated.[9]

To validate and evaluate the performance of our present model, steady flows in axisymmetric constricted tubes are simulated. To investigate its compressibility effect, 3D Womersley flow is also simulated. The 3D Womersley flow (pulsatile flow in aixsymmetric pipe) is driven by periodic pressure gradient at the inlet of the pipe.

In this paper, at the next part, derivation of our accurate axisymmetric model is illustrated in detail. In the third part, the general implementation of the model and boundary conditions are discussed. In the final part, we focus on two particular problems. One is steady flows through constricted axisymmetric tubes. The other is the pulsatile flows in a circular pipe with $120 < \text{Re} < 1200$ (Reynolds number is based on pipe's diameter), Womersley number $3 < \alpha < 9$. The results are all compared with the exact analytical solutions or that of Finite Volume Method. The excellent agreements validate our model.

2. An Accurate Axisymmetric D2Q9 Model

We consider the problems of the laminar internal flow of an incompressible, isotropic liquid in circular pipe with an axis in x direction. For the axisymmetric flow, the

azimuthal velocity u_ϕ and ϕ coordinate derivatives vanish from the incompressible continuity and Navier–Stokes equations.[11] The continuity equation (1) and Navier–Stokes momentum equations (2) in the pseudo-Cartesian coordinates (x, r) are:[11]

$$\frac{\partial u_\beta}{\partial x_\beta} = -\frac{u_r}{r}, \tag{1}$$

$$\frac{\partial u_\alpha}{\partial t} + \frac{\partial u_\beta u_\alpha}{\partial x_\beta} + \frac{u_\alpha u_r}{r} + \frac{1}{\rho_0}\frac{\partial p}{\partial x_\alpha} - \nu\frac{\partial^2 u_\alpha}{\partial x_\beta^2} = \frac{\nu}{r}\frac{\partial u_\alpha}{\partial r} - \frac{u_r}{r}\delta_{\alpha r}, \tag{2}$$

where u_β ($\beta = x, r$) is the two components of velocity. u_α is the velocity u_x or u_r. x_α, x_β means x or r.

Here we would show how above equations can be recovered from our axisymmetric D2Q9 model. To recover above equations, the Chapman-Enskog Expansion is applied. Here an incompressible D2Q9 model is used to derive our axisymmetric model. The 9 discrete velocities of D2Q9 model are as following,

$$\mathbf{e}_i = \begin{cases} (0,0) & i = 0 \\ \left(\cos\left[\frac{(i-1)\pi}{2}\right], \sin\left[\frac{(i-1)\pi}{2}\right]\right)c & i = 1, 2, 3, 4 \\ \sqrt{2}\left(\cos\left[\frac{(i-5)\pi}{2} + \frac{\pi}{4}\right], \sin\left[\frac{(i-5)\pi}{2} + \frac{\pi}{4}\right]\right)c & i = 5, 6, 7, 8 \end{cases}, \tag{3}$$

where $c = \delta_x/\delta_t$, and in our studies $c = 1$. δ_x and δ_t are the lattice spacing and time step size. The evaluation equation describing 2D flow in (x, r) pseudo-Cartesian coordinates is illustrated as Eq. (4):

$$f_i(x + ce_{ix}\delta_t, r + ce_{ir}\delta_t, t + \delta_t) - f_i(x, r, t) = \frac{1}{\tau}[f_i^{\text{eq}}(x, r, t) - f_i(x, r, t)] + h_i(x, r, t) \tag{4}$$

where $f_i(x, r, t)$ is the distribution functions for particles with velocity $\mathbf{e}_i$ at position (x, r) and time t. τ is the relax time constant. The relax time constant τ and the fluid viscosity ν satisfies equation $\nu = (2\tau - 1)\delta_x/6$. Equation (4) is similar to the evaluation equation for D2Q9 model in 2D (x, y) Cartesian coordinates. The difference is that a source term h_i (x, r, t) was incorporated into the microscopic evaluation equation. In Eq. (4), the equilibrium distribution f_i^{eq} of incompressible D2Q9 model[9] is defined by Eq. (5):

$$f_i^{\text{eq}}(x, r, t) = \omega_i\frac{p}{c_s^2} + \omega_i\rho_0\left[\frac{\mathbf{e}_i \cdot \mathbf{u}}{c_s^2} + \frac{(\mathbf{e}_i \cdot \mathbf{u})^2}{2c_s^4} - \frac{\mathbf{u}^2}{2c_s^2}\right] \quad i = 0, 1, 2, \dots, 8, \tag{5}$$

where $c_s = c/\sqrt{3}$, p is the pressure and ρ_0 is the density of fluid. In Eq. (5), for D2Q9 model, $\omega_0 = 4/9$, $\omega_i = 1/9$, ($i = 1, 2, 3, 4$), $\omega_i = 1/36$, ($i = 5, 6, 7, 8$). It is noticed that the main difference between above incompressible D2Q9 model and the standard D2Q9 model is the form of Eq. (5).

To derive our axisymmetric model, here we introduce the following expansions,[9]

$$f_i(x + e_{ix}, r + e_{ir}, t + 1) = \sum_{n=0}^{\infty} \frac{\varepsilon^n}{n!} D^n f_i(x, r, t),$$ (6)

$$\begin{cases} f_i = f_i^{(0)} + \varepsilon f_i^{(1)} + \varepsilon^2 f_i^{(2)} + \cdots \\ \partial_t = \varepsilon \partial_{1t} + \varepsilon^2 \partial_{2t} + \cdots \\ \partial_\beta = \varepsilon \partial_{1\beta} \\ h_i = \varepsilon h_i^{(1)} + \varepsilon^2 h_i^{(2)} + \cdots \end{cases},$$ (7)

where $\varepsilon = \delta_t$ and $D \equiv (\partial_t + e_{i\beta}\partial_\beta)$, $\beta = x, r$ and x_α, x_β means x or r. It is noticed that in Eq. (7), there is no "equilibrium" h_i term.

Retaining terms up to $O(\varepsilon^2)$ in Eqs. (6) and (7) and substituting into Eq. (4) results in:

$$\begin{aligned} &\left\{ [(\varepsilon\partial_{1t} + \varepsilon^2\partial_{2t}) + e_{i\beta}\varepsilon\partial_{1\beta}] + \frac{1}{2}[(\varepsilon\partial_{1t} + \varepsilon^2\partial_{2t})^2 \right. \\ &\left. + 2(\varepsilon\partial_{1t} + \varepsilon^2\partial_{2t})e_{i\beta}\varepsilon\partial_{1\beta} + (e_{i\beta}\varepsilon\partial_{1\beta})^2] \right\} (f_i^{(0)} + \varepsilon f_i^{(1)} + \varepsilon^2 f_i^{(2)}) \\ &= -\frac{1}{\tau}(f_i^{(0)} - f_i^{\text{eq}} + \varepsilon f_i^{(1)} + \varepsilon^2 f_i^{(2)}) + \varepsilon h_i^{(1)} + \varepsilon^2 h_i^{(2)}. \end{aligned}$$ (8)

We can rewrite Eq. (8) in the consecutive order of the parameter ε as following Eqs. (9), (10) and (11) respectively.

$$O(\varepsilon^0) : \frac{(f_i^{(0)} - f_i^{\text{eq}})}{\tau} = 0,$$ (9)

$$O(\varepsilon^1) : (\partial_{1t} + e_{i\beta}\partial_{1\beta})f_i^{(0)} + \frac{1}{\tau}f_i^{(1)} - h_i^{(1)} = 0,$$ (10)

$$O(\varepsilon^2) : \partial_{2t}f_i^{(0)} + (\partial_{1t} + e_{i\beta}\partial_{1\beta})f_i^{(1)} + \frac{1}{2}(\partial_{1t} + e_{i\beta}\partial_{1\beta})^2 f_i^{(0)} + \frac{1}{\tau}f_i^{(2)} - h_i^{(2)} = 0.$$ (11)

The distribution function f_i is constrained by the following relationships:[9]

$$\begin{aligned} \sum_{i=0}^{8} f_i^{(0)} &= \frac{p}{c_s^2}, \quad \sum_{i=0}^{8} e_{i\alpha}f_i^{(0)} = \rho_0 u_\alpha, \\ \sum_{i=0}^{8} f_i^{(m)} &= 0, \quad \sum_{i=0}^{8} \mathbf{e}_i f_i^{(m)} = 0 \text{ for } m > 0. \end{aligned}$$ (12)

Note that $E^{(2n+1)} = 0$ for $n = 0, 1, \ldots$, where $E^{(n)}$ are the tensors defined as $E^{(n)} = \sum_\alpha e_{\alpha 1} e_{\alpha 2} \cdots e_{\alpha n}$ and

$$\sum_{i=1}^{4} e_{i\alpha} e_{i\beta} = 2\delta_{\alpha\beta} ,$$

$$\sum_{i=5}^{8} e_{i\alpha} e_{i\beta} = 4\delta_{\alpha\beta} ,$$

$$\sum_{i=1}^{4} e_{i\alpha} e_{i\beta} e_{i\gamma} e_{i\zeta} = 2\delta_{\alpha\beta\gamma\zeta} , \tag{13}$$

$$\sum_{i=5}^{8} e_{i\alpha} e_{i\beta} e_{i\gamma} e_{i\zeta} = 4\Delta_{\alpha\beta\gamma\zeta} - 8\delta_{\alpha\beta\gamma\zeta} ,$$

where $\delta_{\alpha\beta}$ and $\delta_{\alpha\beta\gamma\zeta}$ are the Kronecker tensors, and

$$\Delta_{\alpha\beta\gamma\zeta} = \delta_{\alpha\beta}\delta_{\gamma\zeta} + \delta_{\alpha\gamma}\delta_{\beta\zeta} + \delta_{\alpha\zeta}\delta_{\beta\gamma} . \tag{14}$$

With above properties of the tensor $E^{(n)}$, we have:

$$\sum_{i=0}^{8} e_{i\alpha} e_{i\beta} f_i^{(0)} = \rho_0 u_\alpha u_\beta + p\delta_{\alpha\beta} , \tag{15}$$

$$\sum_{i} e_{i\alpha} e_{i\beta} e_{ik} f_i^{(0)} = \rho_0 c_s^2 (\delta_{jk}\delta_{\beta\alpha} + \delta_{j\alpha}\delta_{\beta k} + \delta_{j\beta}\delta_{\alpha k}) u_j . \tag{16}$$

2.1. *Mass Conservation and* $h_i^{(1)}$

Summing on i in Eq. (10), we obtain at $\mathrm{O}(\varepsilon)$

$$\partial_{1t}\left(\frac{p}{c_s^2}\right) + \rho_0\partial_\beta u_\beta = \sum_i h_i^{(1)} , \tag{17}$$

which motivates the following selection of $h_i^{(1)}$ when comparing with the target dynamics [of Eqs. (1) and (2)]. Rewriting Eq. (17) in a dimensionless form, we can see that a condition of $L_x/(c_s T) \ll 1$ should be satisfied to neglect the term $\partial_{1t}(p/c_s^2)$,[9] where L_x is the character length in x direction, T is the character time of unsteady flow. That's an additional limit of our derivation besides condition mach number $M \ll 1$.

To recover the continuity Eq. (1), because $\sum_i \omega_i = 1$, the following selection of $h_i^{(1)}$ is reasonable.[3]

$$h_i^{(1)} = -\frac{\omega_i \rho_0 u_r}{r} . \tag{18}$$

Then we proceed to $\mathrm{O}(\varepsilon^2)$ now. Summing on i in Eq. (11) gives

$$\partial_{2t}\left(\frac{p}{c_s^2}\right) + \sum_i \frac{1}{2}(\partial_{1t} + e_{i\beta}\partial_{1\beta})h_i^{(1)} - \sum_i h_i^{(2)} = 0\,. \tag{19}$$

Since[9] $\partial_{2t}(p/c_s^2) = 0$ and with our target dynamics in view, the remaining terms in Eq. (19) should vanish. Hence, we obtain

$$\sum_i h_i^{(2)} = \frac{1}{2}\sum_i(\partial_{1t} + e_{i\beta}\partial_{1\beta})h_i^{(1)}$$

$$= \frac{1}{2}\left[\partial_{1t}\sum_i\left(\frac{-\omega_i\rho_0 u_r}{r}\right)\right] = -\frac{1}{2}\left[\partial_{1t}\left(\frac{\rho_0 u_r}{r}\right)\right]\,. \tag{20}$$

In the above process, we have used the results of $\sum\omega_i e_{i\beta} = 0$.

2.2. *Momentum Conservation and $h_i^{(2)}$*

Multiplying Eq. (10) by $e_{i\alpha}$ and summing on i, gives

$$\rho_0\partial_{1t}u_\alpha + \partial_{1\beta}\Pi_{\alpha\beta}^0 = \sum_i h_i^{(1)}e_{i\alpha} = 0\,, \tag{21}$$

where, $\Pi_{\alpha\beta}^0 = \sum_{i=0}^8 e_{i\alpha}e_{i\beta}f_i^{(0)}$ is the zeroth-order momentum flux tensor. With $\Pi_{\alpha\beta}^0$ given by Eq. (15), using Eq. (21) gives

$$\rho_0\partial_{1t}u_r = -\partial_\beta\Pi_{r\beta}^0 = -\partial_\beta(p\delta_{r\beta} + \rho_0 u_\beta u_r)\,. \tag{22}$$

Substituting Eq. (22) into Eq. (20), we have a condition on the $h_i^{(2)}$.

$$\sum_i h_i^{(2)} = \frac{1}{2r}\partial_\beta(p\delta_{r\beta} + \rho_0 u_\beta u_r)\,. \tag{23}$$

The error in previous model of Halliday *et al.*[3] partly lies in their opinion about Eq. (21). It seems Halliday *et al.* simply regarded that terms $\rho_0\partial_{1t}u_\alpha + \partial_{1\beta}(\rho_0 u_\alpha u_\beta)$ as the terms $D_t u_\alpha = \partial_t u_\alpha + \partial_\beta(u_\beta u_\alpha) + u_\alpha u_r/r$. Unfortunately, that's not true. The term $u_x u_r/r$ which did not consider in the model of Halliday *et al.*[3] plays important role in simulation constricted pipe flows.

Multiplying Eq. (11) with $e_{i\alpha}$ and summing over i gives,

$$\rho_0\partial_{2t}u_\alpha + \left(1 - \frac{1}{2\tau}\right)\partial_{1\beta}\Pi_{\alpha\beta}^{(1)}$$

$$= -\frac{1}{2}\left(\partial_{1t}\sum_i e_{i\alpha}h_i^{(1)} + \partial_{1\beta}\sum_i e_{i\alpha}e_{i\beta}h_i^{(1)}\right) + \sum_i h_i^{(2)}e_{i\alpha}\,, \tag{24}$$

where, $\Pi_{\alpha\beta}^{(1)} = \sum_i e_{i\alpha}e_{i\beta}f_i^{(1)}$ is the first-order momentum flux tensor. With the aid of Eqs. (10) and (16), we have:

$$\Pi_{\alpha\beta}^{(1)} = \sum_i e_{i\alpha}e_{i\beta}f_i^{(1)} = -\tau \sum_i e_{i\alpha}e_{i\beta}D_{1t}f_i^{(0)} + \tau \sum_i e_{i\alpha}e_{i\beta}h_i^{(1)}$$

$$= -\tau \left[\sum_i \partial_{1t}\Pi_{\alpha\beta}^{(0)} + \partial_k \left(\sum_i e_{i\alpha}e_{i\beta}e_{ik}f_i^{(0)} \right) \right] + \tau \sum_i e_{i\alpha}e_{i\beta}h_i^{(1)}$$

$$= -\tau \left[\sum_i \partial_{1t}\Pi_{\alpha\beta}^{(0)} + \rho_0 c_s^2 \left(\delta_{\alpha\beta}\partial_j u_j + \frac{\partial u_\alpha}{\partial x_\beta} + \frac{\partial u_\beta}{\partial x_\alpha} \right) \right] + \tau \sum_i e_{i\alpha}e_{i\beta}h_i^{(1)}. \quad (25)$$

For the first term in Eq. (25), using Eqs. (17) and (21) and the additional condition $L_x/(c_s T) \ll 1$, it can also be rewritten as:

$$\sum_i \partial_{1t}\Pi_{\alpha\beta}^{(0)} = \partial_{1t}(p\delta_{\alpha\beta} + \rho_0 u_\alpha u_\beta) = \delta_{\alpha\beta}\partial_{1t}p + u_\beta\rho_0\partial_{1t}u_\alpha + u_\alpha\rho_0\partial_{1t}u_\beta$$

$$= -u_\beta\partial_k(\rho_0 u_\alpha u_k + p\delta_{k\alpha}) - u_\alpha\partial_k(\rho_0 u_\beta u_k + p\delta_{k\beta}). \quad (26)$$

In above Eq. (26), since $\sum_i \partial_{1t}\Pi_{\alpha\beta}^{(0)}$ are of $O(u^3)$, it can be neglected.[9] Hence, using Eqs. (17) and (18), the second term in LHS of Eq. (24) can be written as:

$$\left(1 - \frac{1}{2\tau} \right) \partial_{1\beta}\Pi_{\alpha\beta}^{(1)}$$

$$= -\tau \left(1 - \frac{1}{2\tau} \right) \rho_0 c_s^2 \left[\partial_{1\beta} \left(\delta_{\alpha\beta}\partial_j u_j + \frac{\partial u_\alpha}{\partial x_\beta} + \frac{\partial u_\beta}{\partial x_\alpha} \right) + \partial_{1\beta} \left(\frac{\delta_{\alpha\beta}u_r}{r} \right) \right]$$

$$= -\nu\rho_0\partial_{1\beta}(\partial_\beta u_\alpha + \partial_\alpha u_\beta). \quad (27)$$

Substituting Eq. (27) into Eq. (24), we move the term $-\rho_0\nu\partial_\alpha(\partial_\beta u_\beta)$ to the RHS of Eq. (24). Rearranging the RHS of Eq. (24) and using results $\sum \omega_i e_{i\beta} = 0$ and $\sum \omega_i e_{i\alpha}e_{i\beta} = c_s^2\delta_{\alpha\beta}$ and Eq. (17), gives

$$\text{RHS} = \frac{1}{2}c_s^2\partial_{1\beta} \left(\frac{\delta_{\alpha\beta}\rho_0 u_r}{r} \right) + \rho_0\nu\partial_\alpha(\partial_\beta u_\beta) + \sum_i h_i^{(2)}e_{i\alpha}$$

$$= c_s^2(1-\tau)\partial_\alpha \left(\frac{\rho_0 u_r}{r} \right) + \sum_i h_i^{(2)}e_{i\alpha}. \quad (28)$$

Hence, incorporating the Eqs. (21), (24), (27) and (28), we get:

$$\rho_0 \left(\frac{\partial u_\alpha}{\partial t} + \frac{\partial u_\beta u_\alpha}{\partial x_\beta} + \frac{\partial p}{\rho_0\partial x_\alpha} - \nu\frac{\partial^2 u_\alpha}{\partial x_\beta^2} \right) = c_s^2(1-\tau)\partial_\alpha \left(\frac{\rho_0 u_r}{r} \right) + \sum_i h_i^{(2)}e_{i\alpha}. \quad (29)$$

Comparing momentum Eq. (29) with Eq. (2), to recover the Navier–Stokes momentum equations, Eq. (30) should be satisfied:

$$c_s^2(1-\tau)\partial_\alpha \left(\frac{\rho_0 u_r}{r} \right) + \sum_i h_i^{(2)}e_{i\alpha} = \frac{\nu}{r} \left(\partial_r\rho_0 u_\alpha - \frac{1}{r}\rho_0 u_r\delta_{r\alpha} \right) - \frac{\rho_0 u_\alpha u_r}{r}. \quad (30)$$

Solving equation system of Eqs. (23) and (30), we can obtain the expression of $h_i^{(2)}$ as following:

$$
h_i^{(2)} = \left(\frac{\omega_i}{2r}\right)[\partial_\beta(p\delta_{r\beta} + \rho_0 u_\beta u_r)]
$$

$$
+ 3\omega_i\left[\left(\frac{\nu}{r}\right)\left(\partial_r \rho_0 u_\beta - \frac{1}{r}\rho_0 u_r \delta_{r\beta}\right)e_{i\beta} - \left(\frac{\rho_0 u_\beta u_r e_{i\beta}}{r}\right)\right]
$$

$$
- \omega_i(1-\tau)\partial_{1\beta}\left(\frac{\rho_0 u_r}{r}\right)e_{i\beta}. \tag{31}
$$

It can also be rewritten as:

$$
\frac{h_i^{(2)}}{\rho_0} = \frac{\omega_i}{2r}\left(\partial_r \frac{p}{\rho_0} + \partial_x u_x u_r + \partial_r u_r u_r\right) + \frac{3\omega_i\nu}{r}(\partial_r u_x + \partial_r u_r)e_{ix} - \frac{3\omega_i\nu}{r^2}u_r e_{ir}
$$

$$
- 3\omega_i\left(\frac{u_x u_r}{r}e_{ix} + \frac{u_r u_r}{r}e_{ir}\right) - \omega_i(1-\tau)\left(\frac{1}{r}\partial_x u_r e_{ix} - \frac{u_r}{r^2}e_{ir} + \frac{\partial_r u_r}{r}e_{ir}\right). \tag{32}
$$

The expression of $h_i^{(1)}$ (Eq. (18)), $h_i^{(2)}$ (Eq. (32)) are successfully derived and the continuity equation (1) and Navier–Stokes equation (2) can be fully recovered.

In the model of Halliday *et al.*,[3] the mainly missing terms are relative to u_r. Although these terms may only slightly affect results of straight pipe flow, without these terms, the flows in constricted pipes can't be simulated correctly.

3. Implementation of the Model and Boundary Condition

3.1. *Implementation of the model*

In numerical simulations, one must ensure that the Mach number is low and the density fluctuation ($\delta\rho$) is of order $O(M^2)$.[9] The additional limit $L_x/(c_sT) \ll 1$ is illustrated in above derivation. In this part, we mainly discuss the how to perform numerical simulation with such a model.

In our aixsymmetric D2Q9 model, $f_i(x,r,t)$ is the distribution function. The macroscopic pressure p and momentum $\rho_0\mathbf{u}$ are defined as:

$$
\sum_{i=0}^{8} f_i = \frac{p}{c_s^2}, \qquad \sum_{i=0}^{8} f_i e_{i\alpha} = \rho_0 u_\alpha. \tag{33}
$$

The two main steps of Lattice BGK model are collision and streaming. In the collision step, a group of calculations (34) and (35) are implemented:

$$
f_i^{ne} = f_i(x,r,t) - f_i^{\text{eq}}(x,r,t), \tag{34}
$$

$$
f_i^+(x,r,t) = f_i^{\text{eq}}(x,r,t) + \left(1 - \frac{1}{\tau}\right)f_i^{ne} + \delta_t h_i^{(1)} + \delta_t^2 h_i^{(2)}, \tag{35}
$$

where f_i^{eq} is the equilibrium momentum distribution function which can be obtained through Eq. (5). f_i^{ne} is the non-equilibrium part of distribution function. $h_i^{(1)}$ and

$h_i^{(2)}$ are the "source" terms added into the collision step, which can calculated through Eqs. (18) and (32) respectively. For simplicity, in our study, $\delta_t = \delta_x$. f_i^+ is the post-collision distribution function.

In the streaming step, the new distribution function value obtained from (35) would propagate to neighbour 8 lattices. That procedure can be represented by the following Eq. (36).

$$f_i(x + e_{ix}\delta_t, r + e_{ir}\delta_t, t + \delta_t) = f_i^+(x, r, t). \tag{36}$$

For the velocity derivations in Eq. (32), the terms $\partial_r u_x + \partial_x u_r$, $\partial_x u_x$ and $\partial_r u_r$ can all be obtained through Eq. (37) with $\alpha = x$, $\beta = r$; $\alpha = \beta = x$; $\alpha = \beta = r$ respectively:

$$\rho_0 \nu (\partial_\beta u_\alpha + \partial_\alpha u_\beta) = -\left(1 - \frac{1}{2\tau}\right) \sum_{i=0}^{8} f_i^{(1)} e_{i\alpha} e_{i\beta}$$

$$= -\left(1 - \frac{1}{2\tau}\right) \sum_{i=0}^{8} f_i^{ne} e_{i\alpha} e_{i\beta} + \mathrm{O}(\varepsilon^2). \tag{37}$$

For the term $\partial_r u_x$ in Eq. (32), it equal to $(\partial_r u_x + \partial_x u_r) - \partial_x u_r$. Since $(\partial_r u_x + \partial_x u_r)$ can be easily obtained by Eq. (37), only value of $\partial_x u_r$ is left unknown to determine $\partial_r u_x$. Here we recourse to finite difference method to obtain $\partial_x u_r$ at lattice node (i, j), which can be calculated by Eq. (38):

$$(\partial_x u_r)_{i,j} = \frac{((u_r)_{i+1,j} - (u_r)_{i-1,j})}{(2\delta_x)}. \tag{38}$$

The values of $\partial_r u_x + \partial_x u_r$, $\partial_x u_x$, $\partial_r u_r$, $\partial_r u_x$ and $\partial_x u_r$ for the lattice nodes which just on the wall boundary can also be calculated from Eqs. (37) and (38). Obtaining these values for lattice nodes on the periodic boundary is also easy. However, to obtain these values for the nodes on the inlet/outlet pressure-specified boundary, these values are extrapolated from those of the inner nodes.

3.2. *Boundary condition*

For wall boundary condition, it is well known that the most commonly applied in LBM is bounce back model.[4] However, to treat the curvature wall boundary in uniform suqare lattices, original bounce back model is not accurate enough for curvature boundary. Here, the non-equilibrium distribution function extrapolation method[12] was applied for curvature wall boundary. In the method, the velocity on "wall nodes" (lattice nodes outside and most near to physical boundary) is obtained from extrapolation and p value obtained from the nearest "fluid node"(lattice nodes inside physical boundary), hence the equilibrium distribution function for "wall nodes" can be obtained through Eq. (5). With corresponding non-equilibrium distribution function extrapolated from the "fluid nodes", the collision step on "wall nodes" can be fulfilled. This treatment is proved to be second order in space.[12]

For the inlet/outlet boundary conditions, the pressure or velocity boundary condition treatments have been proposed by previous LBM studies.[13,14] Here the scheme proposed by Guo, *et al.*[13] was adopt for its simplicity. To specify pressure at inlet/outlet boundary, the corresponding velocity value in these boundaries was extrapolated from the next inner nodes. Hence, the equilibrium part of distribution function can be determined through above Eq. (5) and the non-equilibrium part of distribution function can be obtained through extrapolation.[13] So, the collision step for boundary nodes can be implemented normally as inner nodes. Specifying the velocity boundary condition is similar.

For 3D Womersley flow simulation, another scheme can implement the uniform oscillatory pressure gradient except scheme of inlet/outlet pressure specify. That is applying an equivalent oscillatory body force.[15] To apply an equivalent body force, the periodic boundary conditions are imposed at the open ends of the pipe and in the collision step, after step (35) was implemented, a further post collision step is necessary:

$$f_i^+(x, r, t) = f_i^+(x, r, t) + \omega_i F_\alpha \frac{e_{i\alpha}}{c_s^2}, \qquad i = 1, 2, \ldots, 8. \tag{39}$$

Where $\mathbf{F} = (p^* \cos(\omega t), 0)$ is the body force. p^* is the maximum amplitude of the oscillatory pressure gradient.

4. Results and Discussion

4.1. *Steady flow through constricted pipes*

In our study, geometry of the constrictions is described by Cosine curve. The geometry of two stenoses is shown in Fig. 1. If r_0 is the radius of the nonstenotic part of the pipe, radius of the first stenose $r(x)$ is given in function below.

$$r(x) = r_0 - \frac{\beta r_0 \{1 + \cos[\pi x/S_0]\}}{2} (-S_0 < x < S_0). \tag{40}$$

Where $r_0 = D/2$, $\beta = 50$ is severity of stenose and the axial length of the stenose is $2S_0$. To make flow fully developed and save grid nodes, length between the right end and the stenose is $S_2 = 8D$ and $S_1 = 3D$ as illustrated in Fig. 1. In this part, the steady flows through constricted tubes are studied.
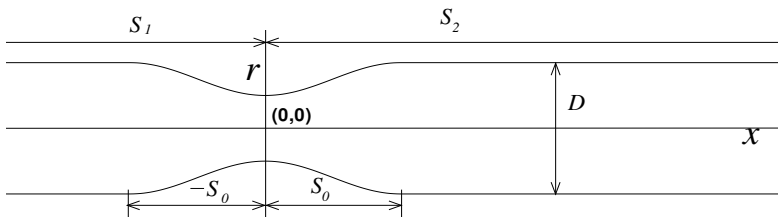

Fig. 1.   Geometry of constricted tubes.

In our simulations, the zero velocities are initialized everywhere. At the inlet boundary, a fully developed parabolic velocity profile is specified. In the outlet boundary, the outlet pressure was specified and $\partial \mathbf{u}/\partial x = 0$ was also imposed. In our study, for defining steady state, our criterion is:

$$\sum_{i,j} \frac{\| \sqrt{[u_x(x_i, r_j, t+1) - u_x(x_i, r_j, t)]^2 + [u_r(x_i, r_j, t+1) - u_r(x_i, r_j, t)]^2} \|}{\| \sqrt{[u_x(x_i, r_j, t+1)]^2 + [u_r(x_i, r_j, t+1)]^2} \|}$$

$$< 10^{-6}, \tag{41}$$

where i, j are the lattice nodes index.

Firstly we simulated the case of $S_0 = D$, Reynolds number defined as Re = $U_0 D/\nu$, where U_0 is central value of the inlet parabolic velocity. We also notice that to calculate Formula (32), there is a singularity ($r = 0$) for lattices located in the axis. To avoid the singularity, the axis should be located off lattices. Hence, for simplicity, the axis is located in middle of two center horizontal lattice rows. In the simulation totally $N_x \times N_r = 441 \times 42$ lattices (area: $440\delta_x \times 42\delta_x$) was applied. The diameter is $D = 40\delta_x$, where $\delta_x = 1$. To validate our results, the same case was also simulated by Finite Volume method (FVM) with very fine meshes.

In Fig. 2, the velocity profiles in positions $x = 0$, $0.5D$, D and $2D$ are all compared with that of FVM. Both the axial and radial velocity components agree well with that of FVM. That validates our derived formulas. Since the axis locate off lattices and $r = 20\delta_x$, the nonstenotic wall is also located off lattices. From Fig. 2 we can see that although there are no lattices locate at position $(x/D, r/D) = (0, 0.25)$, the wall boundary condition can still ensure the zero velocity at that position.

A more serious constriction case are also studied, in the case $S_0 = D/2$, Re = 10. Comparison of the axial and radial velocity profiles in different position is illustrated in Fig. 3. Our results are also in consistent with that of FVM. It seems that with just 42 lattice represent nonstenotic diameter can also achieve accurate results.
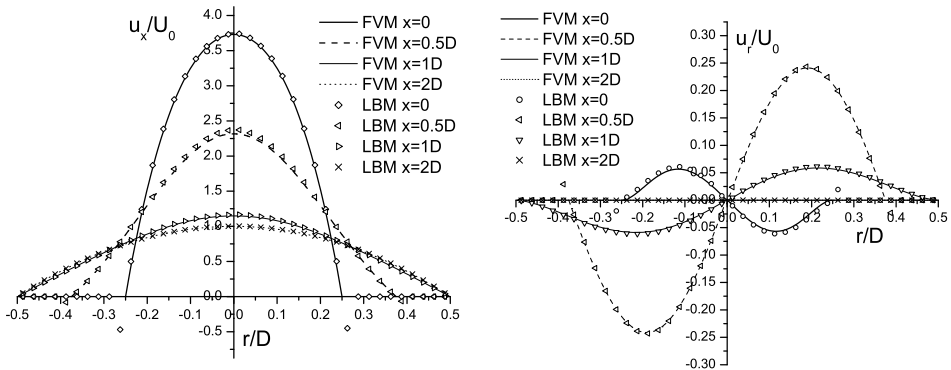

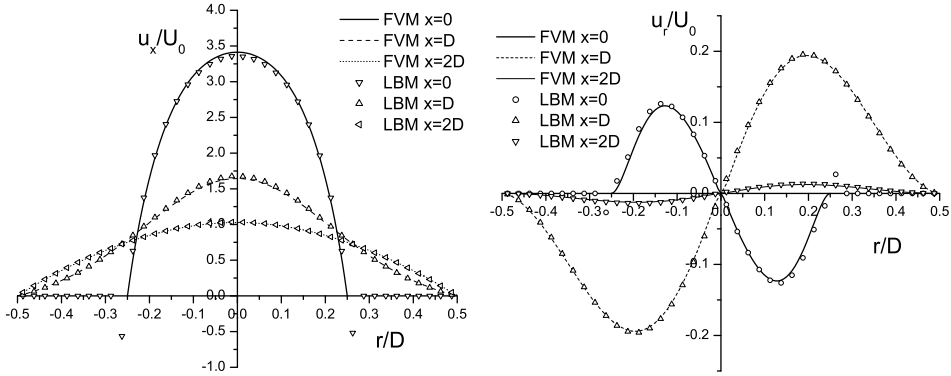Fig. 2. Velocity profiles in different position in case of $S_0 = D$, Re = 10.

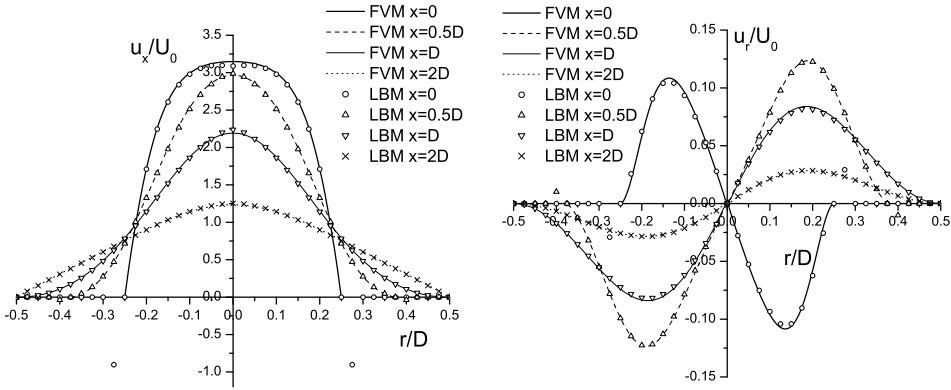Fig. 3.   Velocity profiles in different position in case of $S_0 = D/2$, Re = 10.

Fig. 4.   Velocity profiles in different position in case of $S_0 = D$, Re = 50.

In above case we obtained correct results using the method of avoiding singularity. Through asymptotic analysis, we also observed that when the central lattice nodes lie in the axis, using formulas below can also achieve correct results.

$$h_{i,jcen}^{(1)} = -\frac{\omega_i \rho_0 (u_r)_{jcen+1}}{r_{jcen+1}}, \qquad h_{i,jcen}^{(2)} = \frac{(h_{i,jcen+1}^{(2)} + h_{i,jcen-1}^{(2)})}{2}. \qquad (42)$$

Appling the Eq. (42) we obtain the results for case $S_0 = D$, Re = 50. The velocity profile comparison is illustrated in Fig. 4. It seems the results are also very good.

Because previous model of Halliday, *et al.*[3] missing some important terms relative to radial velocities, it is observed neither the axial nor the radial velocity profiles are correct. Figure 5 illustrated that problem. Form the figure we can see that even very fine lattices $N_x \times N_r = 881 \times 83$ was applied, the model of Halliday, *et al.*[3] can only give out poor results comparing with results of FVM. However, in the circumstances of straight tube, u_r is so small that the missing terms are almost
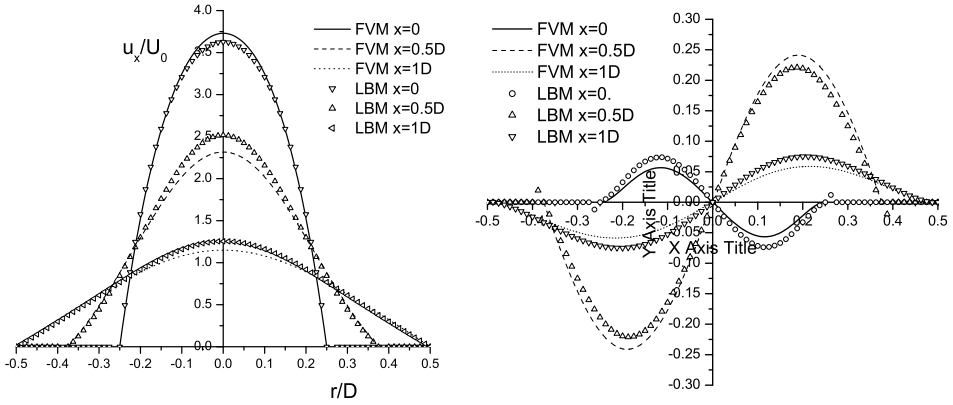
Fig. 5. Results obtained from model of Halliday *et al.*[3] for case of $S_0 = D$, Re $= 10$.

can be neglected. So Halliday, et al. also got valid result for straight circular tube.[3] In the next part of our discussion, we can see the Halliday's model can also give out some accurate results for 3D Womersley flow which is unsteady flow through straight tube.

4.2. *Unsteady tube flow (3D Womersley flow)*

The 3D Womersley Flow (pulsatile flow in aixsymmetric pipe) is driven by periodic pressure gradient at the inlet of the pipe. In the following, p^* is the maximum amplitude of the sinusoidally varying pressure gradient.

$$\frac{\partial p}{\partial x} = -p^* e^{i\omega t} \,. \tag{43}$$

R is defined as the radius of the circular pipe. ω is the angular frequency and ν is the kinetic viscosity of fluid. The Reynolds number is defined as Re $= 2U_s R/\nu$, U_s is the velocity defined as:

$$U_s = \frac{p^* \alpha^2}{4\omega\rho} = \frac{p^* R^2}{4\rho\nu} \,, \tag{44}$$

which is the velocity that would be observed at the centre of the tube if a constant forcing term p^* were applied in the limit of $\alpha \to 0$ (steady flow). The Womersley number is defined as $\alpha = R\sqrt{\omega/\nu}$. The Strouhal number is defined as $St = R/(U_s T)$, where T is the sampling period.

The analytical solution for aixsymmetric pipe pulsatile flow[4] is:

$$u(r,t) = \text{Re}\left\{ \frac{p^*}{i\omega\rho_0} \left[1 - \frac{J_0[1/\sqrt{2}(-\alpha + i\alpha)r/R]}{J_0[1/\sqrt{2}(-\alpha + i\alpha)]} \right] e^{i\omega t} \right\} \,, \tag{45}$$

where J_0 is the zeroth order Bessel function of the first type.

All the simulations in this part began with an initial condition of zero velocity every where, and an initial run of $10T$ steps.
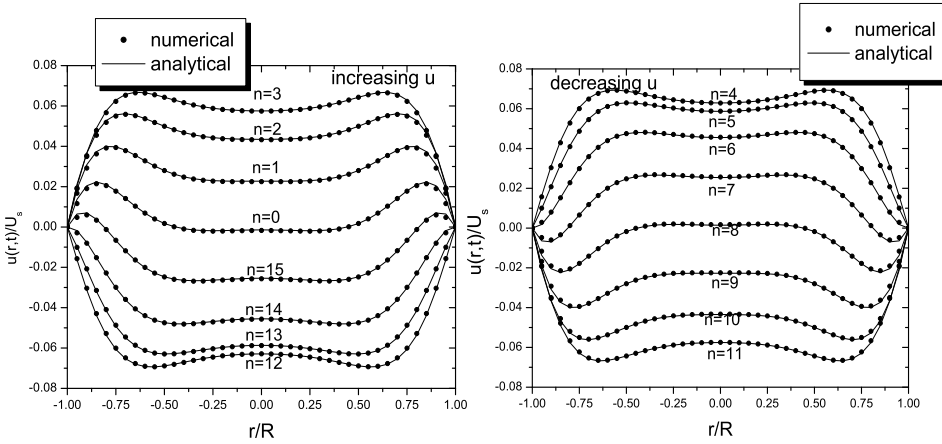
Fig. 6.   Profiles of increasing (left) and decreasing (right) velocities along the diameter of a tube for $\alpha = 7.927$, $T = 1200$, Re $= 1200$, $\tau = 0.6$, at $t = nT/16$ $(n = 0, \ldots, 15)$ $U_s = 1.0$, $U(_{\max} \sim 0.07)$.

It should be noticed that the maximum velocity $U_{\max}$ appearing in tube axis during a sampling period would be less than character velocity U_s for case $\alpha > 0$. For case $\alpha \gg 1$, the $U_{\max}$ would be much less than U_s. It seems when oscillatory pressure gradient changes very fast and it is impossible for velocity field to reach the fully developed velocity profile with maximum value U_s.

A typical Reynolds number in the abdominal aorta is 1250 and a typical Womersley number $\alpha = 8$,[4] firstly simulation the case of Re $= 1200$, $\alpha = 7.93$, $T = 1200$, $\tau = 0.6$ was performed. $N_x \times N_r = 81 \times 41$ and the corresponding $U_s = 1.0$. The exact analytical solutions of Eq. (43) were compared to numerically evaluated velocity profiles along the diameter in Fig. 6. The velocity is normalized by U_s. The r-axis is nondimensionalized by dividing by the radius of the tube as indicated in Fig. 6. Although in this case $U_s = 1.0$, the $U_{\max}$ observed in whole oscillatory period is only about 0.063, $M = 0.063\sqrt{3} \approx 0.109 \ll 1$, which is consistent with the limit of LBM. In all our cases, the additional limit $L_x/(c_sT) \gg 1$ was also satisfied.

Then we'd like to discuss the spatial accuracy of our model through evaluate the error between the numerical and analytical solution. In this study and above cases, the oscillatory pressure is implemented by adding equivalent oscillatory body force. A velocity error formula is introduced as (46). At each time step the error can be defined as:

$$\xi = \frac{\sum_i |u(r_i) - u_a(r_i)|}{\sum_i |u_a(r_i)|}, \tag{46}$$

Where $u(r_i)$ is the numerical solution, $u_a(r_i)$ is the analytical velocity at r_i in middle pipe. The overall average error $\langle \xi \rangle$ is averaged over the period T. For all the
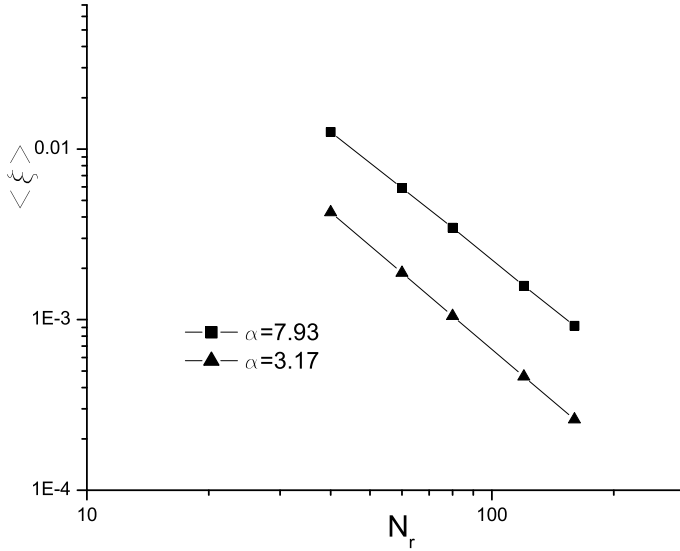
Fig. 7.   Global error $\langle \xi \rangle$ as a function of the pipe diameter N_r for $\alpha = 7.93$ and $\alpha = 3.17$.

cases in this part, the convergence criterion was set as following:

$$\frac{\sum_{\mathbf{x}} |u(\mathbf{x}, t + T) - u(\mathbf{x}, t)|}{\sum_{\mathbf{x}} |u(\mathbf{x}, t + T)|} \leq 10^{-6} \tag{47}$$

where $\mathbf{x}$ is any lattice in computational domain. t usually chosen as $t = 1 + nT$.

Here in all of cases, the pipe length was chosen as $2N_r$, where N_r is the number of lattice nodes in the diameter (usually N_r excludes the up and lower extra layers outside the wall boundary). The global errors behavior for $\alpha = 7.93$ and $\alpha = 3.17$ was illustrated in Fig. 7. For a certain α, as N_r was increased α was kept constant by varying the period T accordingly within the range $T > 10^3$. For above α, the corresponding τ was kept 0.6 and 1.0 respectively. In Fig. 7, the solid lines represent the linear fits, and the slope of the lines are -1.89 ($\alpha = 7.93$) and -2.02 ($\alpha = 3.17$). The figure demonstrates that, current LBGK model incorporating the extrapolation wall boundary condition and the forcing term, is second order in space.

In last part we'd like to find some clues of compressibility effect through investigating the velocity field error. Here to investigate the velocity field error, four cases with $\alpha = 3.963$, $N_x \times N_r = 41 \times 41$, $T = 4800$ were simulated using both present model and the Halliday's model. The scheme of specifying inlet/outlet pressure was chosen to implement pressure gradient. Table 1 shows the velocity field error measured by θ and $\langle \theta \rangle$. θ at time t is defined as:

$$\theta = \frac{\sum_i (u(r_i, t) - u_a(r_i, t))^2}{\sum_i u_a^2(r_i, t)}, \tag{48}$$

where the summation is over the diameter in middle pipe and the overall average error $\langle \theta \rangle$ is averaged over the period T. The $\theta_{\max}$ means the maximum value of θ

Table 1.　The error of velocity field in 3D Womersley flow.

Cases	Re	$p*$	M_{max}	Halliday's model		Present model	
				θ_{max}	$\langle\theta\rangle$ (%)	θ_{max}	$\langle\theta\rangle$ (%)
1	120	0.0001	0.054	0.00534	0.054	0.00481	0.042
2	240	0.0002	0.108	0.0131	0.172	0.0127	0.139
3	600	0.0005	0.272	0.0942	0.923	0.0557	0.730
4	1200	0.001	0.544	0.453	3.39	0.206	2.48

in a sampling period. In Table 1, the M_{max} in tube axis for case 1 to 4 are 0.054, 0.108, 0.272 and 0.544, respectively.

Through comparison of the maximum particular velocity error and the overall numerical average errors of two models in Table 1, we observed that as M_{max} in tube axis increase, the corresponding errors of Halliday's increases faster than present incompressible model. The observation is consistent with conclusion got for the standard and incompressible D2Q9 models.[9] Hence, comparing with Halliday's model, present model can eliminate the compressibility effect.

5. Conclusion

An accurate axisymmetric incompressible LBGK model was derived in this paper by introducing an additional source term to an incompressible LBGK model. With limit of mach number $M \ll 1$ and $L_x/(c_s T) \ll 1$, this axisymmetric LBGK model successfully recovered the Navier–Stokes equation in the cylindrical coordinates through Chapman Enskog expansion. For the additional source term in our model, most velocity gradient terms can be obtained from high order momentum of distribution function, which is consistent with the philosophy of the LBM. The axisymmetric incompressible LBGK model was successfully applied to simulate the steady and unsteady axisymmetric flow in circular tubes.

For studies of steady flow through constricted tubes, because our model can fully recover the continuity and Navier–Stokes equations, accurate results were obtained. For studies of 3D Womersley flow, current LBGK model incorporating the extrapolation boundary condition is of second order in space. Comparing with Halliday's axisymmetric model, it is observed that the present model can reduce the compressibility effect.

References

1. G. McNamara and G. Zanetti, *Phys. Rev. Lett.* **61**, 2332 (1988).
2. F. Higuera and J. Jimenez, *Europhys. Lett.* **9**, 663 (1989).
3. I. Halliday, L. A. Hammond, C. M. Care, K. Good and A. Stevens, *Phys. Rev. E* **64**, 011208 (2001).
4. A. M. Artoli, A. G. Hoekstra and P. M. A. Sloot, *Int. J. Mod. Phys. C* **13**, 1119 (2002).
5. R. S. Maier, R. S. Bernard and D. W. Grunau, *Phys. Fluids* **8**, 1788 (1996).

6. R. Mei, W. Shyy, D. Yu and L. S. Luo, *J. Comput. Phys.* **161**, 680 (2000).
7. U. Frisch, D. d'Humieres, B. Hasslacher, P. Lallemand, Y. Pomeau and J. P. Rivet, *Complex Syst.* **1**, 649 (1987).
8. S. Hou and Q. Zou *et al.*, *J. Comput. Phys.* **118**, 329 (1995).
9. X. He and L. Luo, *J. Stat. Phys.* **88**, 927 (1997).
10. S. Marconi, B. Chopard and J. Latt, *Int. J. Mod. Phys. C* **14**, 1015 (2003).
11. L. D. Landau and E. M. Lifschitz, *Fluid Mechanics*, 2nd edn. (Pergamon, Oxford, 1987).
12. Z. Guo, C. Zheng and B. Shi, *Phys. Fluids* **14**, 2007 (2002).
13. Z. Guo, C. Zheng and B. Shi, *Chinese Physics* **11** (2002).
14. Q. Zou and X. He, *Phys. Fluids* **9**, 1591 (1997).
15. J. A. Cosgrove, J. M. Buick, S. J. Tonge *et al.*, *J. Phys. A*: *Math. Gen* **36**, 2609 (2003).